Check for updates

Small

NANO · MICRO small
www.small-journal.com

RESEARCH ARTICLE OPEN ACCESS

Enantiopurity-Dependent Peptide Coacervates and Asymmetric Organocatalysis

Alice Vetrano[1] | Nico di Fonte[1] | Olivier Monasson[2,3] | Federico Perrella[1] | Martina Porco[1,4] | Ferdinando Mercuri[1] | Gianluca Dell'Orletta[1] | Francesco Petragnano[5] | Alessio Carioscia[1,4] | Davide Deodato[6] | Damiano Calcagno[7] | Giovanna Salvitti[1] | Samantha Reale[1] | Fabio Pesciaioli[1,4] | Carino Ferrante[8] | Davide Tedeschi[1] | Giuseppe Grasso[6] | Paola Benassi[1] | Elisa Peroni[2,3] | Armando Carlone[1,4] | Isabella Daidone[1] | Claudio Iacobucci[1]

[1]Department of Physical and Chemical Sciences, University of L'Aquila, L'Aquila, Italy | [2]CNRS, BioCIS, C.Y. Cergy Paris Université, Cergy Pontoise, France | [3]CNRS, BioCIS, Université Paris-Saclay, Orsay, France | [4]Consorzio C.I.N.M.P.I.S., INSTM RU, L'Aquila, Italy | [5]Department of Biotechnological and Applied Clinical Sciences, University of L'Aquila, L'Aquila, Italy | [6]Department of Chemical Sciences, University of Catania, Catania, Italy | [7]IRCCS-Fondazione Bietti, Rome, Italy | [8]CNR- SPIN, C/O Department of Physical and Chemical Sciences, University of L'Aquila, L'Aquila, Italy

Correspondence: Armando Carlone (armando.carlone@univaq.it) | Isabella Daidone (isabella.daidone@univaq.it) | Claudio Iacobucci (claudio.iacobucci@univaq.it)

Received: 5 December 2025 | **Revised:** 26 January 2026 | **Accepted:** 2 February 2026

Keywords: chirality | coacervates | liquid-liquid phase separation | LLPS | supramolecular chemistry

ABSTRACT

Membraneless compartmentalization via liquid–liquid phase separation (LLPS) has emerged as a powerful strategy to organize biochemical reactions. Recently, peptide-based coacervates demonstrated the potential to function as microreactors by enhancing reaction kinetics through increased local concentrations and altered microenvironments. Here, we introduce an O-methylated diphenylalanine-based tripeptide ^{LLL}PFF-OCH$_3$ containing an N-terminal proline, designed to undergo LLPS, and simultaneously function as an enantioselective organocatalyst. Comprehensive characterization via confocal microscopy, fluorescence recovery after photobleaching (FRAP), micro-Raman and attenuated total reflection infrared (ATR-IR) spectroscopy, diffusion-surface plasmon resonance (*D*-SPR), and molecular dynamics (MD) simulations revealed the formation of stable liquid droplets. In contrast, a racemic mixture of ^{LLL}PFF-OCH$_3$ and ^{DDD}PFF-OCH$_3$ failed to form liquid droplets and instead formed a solid precipitate, unveiling a critical role of enantiopurity in LLPS. Proof-of-concept catalytic studies proved enantioselective organocatalytic activity of the ^{LLL}PFF-OCH$_3$ liquid coacervates. Beyond catalysis these results may have broader implications in understanding prebiotic chemistry and neurodegeneration.

1 | Introduction

Biological systems rely on the spatial and temporal organization of chemical processes. While membrane-bound organelles serve this function in modern cells, many essential reactions occur in dynamic, membraneless compartments formed through liquid–liquid phase separation (LLPS) [1]. These biomolecular condensates serve to concentrate specific molecules and can modulate reaction kinetics and specificity [2]. Bioinspired by these phenomenon, peptide-based coacervates have recently been introduced as synthetic analogues of biomolecular condensates [3–7]. Composed of short sequences, such as *O*-methylated diphenylalanine derivatives [8], these coacervates can solubilize hydrophobic compounds and enzymes in water, acting as supramolecular microreactors [8, 9]. Previous studies have shown that encapsulating enzymes or catalysts within peptide

Alice Vetrano and Nico di Fonte equally contributed to this work.

This is an open access article under the terms of the Creative Commons Attribution License, which permits use, distribution and reproduction in any medium, provided the original work is properly cited.

© 2026 The Author(s). *Small* published by Wiley-VCH GmbH

droplets can accelerate chemical transformations due to local concentration effects and changes in rate constants [10].

Proline-based peptides have been used in organocatalysis [11], with their self-assembly into gels and fibrils providing structural environments that modulate and support catalysis; indeed, we have recently shown that organocatalytic fibrils, self-assembled from minimal peptides, accelerate catalysis compared to their non-supramolecular organized counterparts [12, 13].

In this work, we introduce a tripeptide that both undergoes LLPS and is a competent enantioselective organocatalyst itself. By integrating L-proline at the N-terminus of an *O*-methylated diphenylalanine-based scaffold we developed the tripeptide ^{LLL}PFF-OCH$_3$, capable of forming chiral liquid droplets that function as asymmetric microreactors in aqueous environments. We characterized these systems at a molecular level using an integrative bioanalytical and computational approach, including confocal microscopy, FRAP, micro-Raman and ATR-IR spectroscopy, *D*-SPR, and MD simulations. Catalytic tests on a model aldol reaction revealed the enantioselective effect of the chiral coacervates. Strikingly, the racemic and scalemic tripeptide failed to undergo LLPS, instead leading to immediate precipitation. Here, "racemic" denotes a 1:1 mixture of two enantiomers, whereas "scalemic" refers to a non-racemic mixture with an excess of one enantiomer. This suggests that enantiopurity may be a prerequisite for spontaneous LLPS and compartmentalization in aqueous environments.

It is worth noting that the enantiopurity-dependent LLPS reported here involves the self-assembly of a single, short peptide. This is conceptually distinct from previous studies, such as those by Perry and co-workers, where LLPS was observed only when mixing oppositely charged polypeptides, and only if at least one was heterochiral, i.e., an optically inactive polymer with randomly distributed D- and L-monomers leading to a statistical mixture of diastereomers [14]. In contrast, our system demonstrates that enantiopurity can be itself a prerequisite for LLPS of a single homochiral peptide. In other words, LLPS in our system is driven by stereodefined supramolecular packing of a single enantiopure tripeptide, rather than by heterochiral polyelectrolyte complexation between acidic and basic peptides.

2 | Results and Discussion

Solubilizing ^{LLL}PFF-OCH$_3$ (Figure 1a) in water yielded a slightly acidic (pH ~ 6), transparent solution (Figure 1b,c). Upon increasing the pH above 7.5, the solution turned turbid and white (Figure 1b,d). Microscopy experiments revealed that the turbidity corresponded to the LLPS of spherical coacervates formed by the concentrated tripeptide, with droplet diameters of approximately 5 μm (Figure 1d,g). Droplet formation was fully reversible upon repeated pH cycling, indicating the dynamic nature of the phase separation process (Figure 1i).

We systematically investigated the LLPS behavior of ^{LLL}PFF-OCH$_3$, evaluating its phase stability and responsiveness to changes in peptide concentration, pH, and temperature. To delineate the phase transition boundaries, we constructed concentration–pH and temperature–pH phase diagrams (Figure 1b). LLPS was observed at concentrations above 2.5 mg·mL^{-1} and within a pH range of ~ 7.5 to 12, with lower temperatures further promoting phase separation. Above pH 12 the turbidity reduced and solid-like particles of ~ 1 μm became visible (Figure 1e). These LLPS conditions are consistent with those reported for the LLPS of ^{LL}FF-OCH$_3$, suggesting that the presence of a C-terminal proline in the tripeptide has minimal influence on droplet formation [8].

The LLPS mechanism proposed for ^{LL}FF-OCH$_3$ likely remains valid: attractive π–π interactions between the aromatic rings of the FF core drive assembly, while repulsive electrostatic interactions involving the partially positively charged N-termini help maintain solubility and define the pH responsiveness of the system. Experimental evidences supporting this hypothesis will be presented later in this paper.

Beyond the morphological characterization, we investigated the internal dynamics of the droplets using FRAP (Figure 1h). Complete fluorescence recovery within ~ 60 s post-bleaching indicates high internal molecular mobility, consistent with the liquid-like nature of the coacervates. Accordingly, coacervate coalescence has been observed (Figure S1).

The liquid droplets formed by ^{LLL}PFF-OCH$_3$ at pH 8.5 proved stable for days (Figure 1j) and under conditions typically disruptive for non-covalent peptide–peptide interactions, including 1 M NaCl, 2 M urea, and up to 40% acetonitrile, above which the turbid solution reverts to transparency.

We applied D-SPR analysis [15, 16]; to characterize the diffusive behavior of 0.5 and 8 mg·mL^{-1} solutions of ^{LLL}PFF-OCH$_3$ at pH 6 and 8.5. At 0.5 mg·mL^{-1}, below the coacervation threshold (Figure 1b), solutions remained transparent at both pH values, and a single diffusion coefficient of ~ $3.5{\cdot}10^{-10}$ m^2·s^{-1} was observed (Figure S2), consistent with low-molecular-weight species. A comparable value was detected for the transparent 8 mg·mL^{-1} solution at pH 6. Notably, at 8 mg·mL^{-1} and pH 8.5, where coacervation occurs, an additional slower diffusing population emerged with a diffusion coefficient of ~ $5.9{\cdot}10^{-11}$ m^2·s^{-1} (Figure S2), indicative of higher molecular weight species. These accounted for ~ 20% of the total diffusion signal [17], suggesting that most peptides remain in minimal-size oligomers, consistent with the transient and dynamic interactions driving LLPS [18].

We next investigated the effect of enantiopurity on the LLPS behavior of the tripeptide. Unlike proteins undergoing LLPS, which are inherently enantiopure, synthetic short peptides offer the opportunity to examine whether enantiomeric excess itself influences LLPS. To this end, we prepared a racemic mixture by combining equal volumes of ^{LLL}PFF-OCH$_3$ and ^{DDD}PFF-OCH$_3$, each at 10 mg·mL^{-1} in water at pH 6, resulting in a final solution containing 5 mg·mL^{-1} of each enantiomer (10 mg·mL^{-1} total peptide concentration).

The resulting racemic solution remained transparent at pH 6, just like the two enantiopure solutions. Notably, this racemic mixture lies at the center of the LLPS region in the phase diagram for pH > 7.5, both in terms of total peptide concentration and individual enantiomer concentration. However, upon adding a

16136829, 0, Downloaded from https://onlinelibrary.wiley.com/doi/10.1002/smll.202514872 by Giuseppe Grasso - Universita Di Catania , Wiley Online Library on [16/02/2026]. See the Terms and Conditions (https://onlinelibrary.wiley.com/terms-and-conditions) on Wiley Online Library for rules of use; OA articles are governed by the applicable Creative Commons License

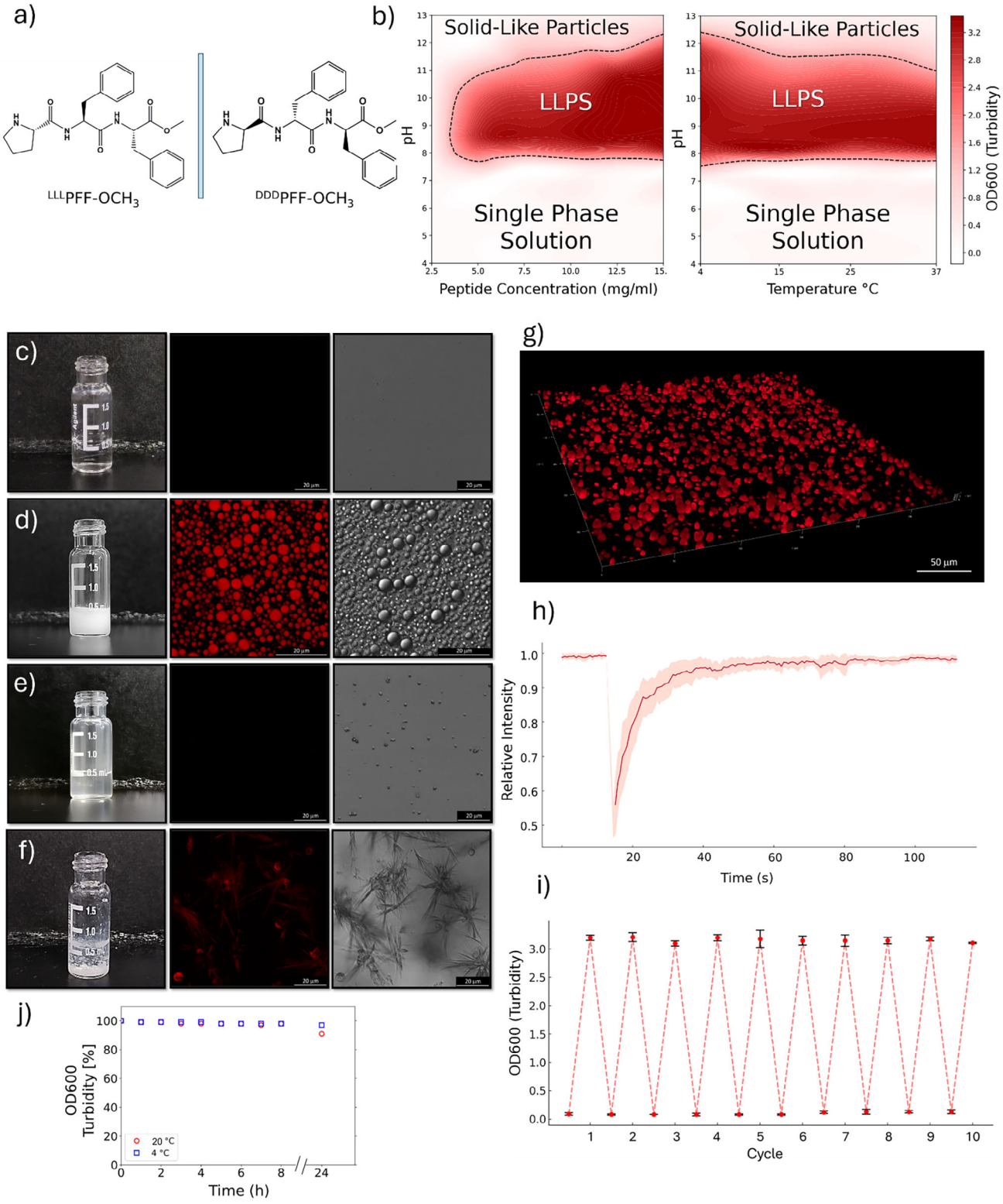

FIGURE 1 | Phase behavior and morphology of PFF-OCH_3 coacervate and solid aggregates. a) Chemical structure of ^{LLL}PFF-OCH_3 and ^{DDD}PFF-OCH_3. b) Phase diagrams depicting the formation of peptide droplets as a function of peptide concentration vs pH (left) and temperature vs pH (right), determined by turbidity (OD600). The LLPS region (dark red) is separated from the single phase solution and from the solid-like particles suspension by dashed boundaries. c–f) Vial appearance, autofluorescence confocal image, and micrograph (scale bar = 20 µm) of 10 mg mL^{-1} solutions of: c) ^{LLL}PFF-OCH_3 at pH 6; d) ^{LLL}PFF-OCH_3 at pH 8.5; e) ^{LLL}PFF-OCH_3 at pH 13; f) racemic (1:1) mixture of ^{LLL}PFF-OCH_3 and ^{DDD}PFF-OCH_3 at pH 8.5. g) 3D autofluorescence confocal reconstruction of ^{LLL}PFF-OCH_3 coacervates (10 mg mL^{-1}, pH 8.5). h) FRAP plot of ^{LLL}PFF-OCH_3 coacervates (10 mg mL^{-1}, pH 8.5) over time. The solid line and shaded area represent the mean and standard deviation over six replicates, respectively. i) Reversibility of LLPS over ten cycles of pH change between 6 and 8. Error bars represent the standard deviation of turbidity from three replicates. j) Stability of ^{LLL}PFF-OCH_3 coacervates (10 mg mL^{-1}, pH 8.5, 4 and 20°C) over time, monitored as the percentage of initial turbidity.

16136829, 0, Downloaded from https://onlinelibrary.wiley.com/doi/10.1002/smll.202514872 by Giuseppe Grasso - Universita Di Catania , Wiley Online Library on [16/02/2026]. See the Terms and Conditions (https://onlinelibrary.wiley.com/terms-and-conditions) on Wiley Online Library for rules of use; OA articles are governed by the applicable Creative Commons License

precise amount of NaOH to adjust the solution to pH 7.5, the system did not undergo LLPS by turning turbid but instead underwent a liquid-to-solid transition, forming large, suspended white flocculent aggregates while remaining optically transparent in the bulk phase (Figure 1f). The racemic mixture obtained by combining equal volumes of ^{LL}FF-OCH$_3$ and ^{DD}FF-OCH$_3$, under the same concentration and condition, also did not undergo LLPS like the enantiopure ^{LL}FF-OCH$_3$ [8] but resulted in immediate precipitation.

To further explore the role of enantiopurity, we prepared scalemic mixtures at 2:1 and 1:2 ratios of ^{LLL}PFF-OCH$_3$ and ^{DDD}PFF-OCH$_3$, keeping the total peptide concentration constant at 10 mg·mL^{-1}. At pH 6, both solutions were transparent. Upon adjusting the pH to 7.5, the scalemic mixtures turned white and turbid, exhibiting suspended flocculent aggregates, similar to the racemic solution. Upon precipitation, the solid aggregates were separated by sedimentation, leaving a PFF-OCH$_3$ excess in solution at 3.3 mg·mL^{-1}, a concentration at which LLPS is expected (Figure 1b). Microscopy of the supernatants revealed the presence of spherical peptide droplets (Figure S3). This behavior is consistent with spontaneous enantiomeric self-disproportionation (SDE), a phenomenon in which scalemic mixtures separate into an enantioenriched solution and a racemic precipitate [19]. We propose that this stereochemical fractionation represents an intrinsic property of the system, emerging independently of any catalytic function. As such, the observation of SDE in peptide-based LLPS is of fundamental interest in its own right and may bear implications for the origins of homochirality [19, 20]. The catalytic activity of the peptide droplets, which may further contribute to such an effects, will be discussed later in this manuscript.

Collectively, these results demonstrate that ^{LLL}PFF-OCH$_3$ undergoes robust and reversible LLPS above pH 7.5, forming liquids. Importantly, enantiopurity emerges as a critical factor: racemic and scalemic mixtures fail to undergo LLPS and instead exhibit spontaneous enantiomeric self-disproportionation, revealing a stereochemistry-based mechanism of phase separation.

Next, we investigated whether the conformational ensemble of ^{LLL}PFF-OCH$_3$ varies as a function of pH and enantiopurity. To this end, we adopted an integrative approach combining micro-Raman and IR spectroscopy, which provide complementary structural insights into both liquid and solid states. We recorded micro-Raman and IR spectra of ^{LLL}PFF-OCH$_3$ under three conditions: in solution before LLPS (pH 6), upon LLPS on single droplets (pH 8.5), and as a solid racemic mixture.

First, we compared the Raman spectrum of the transparent 10 mg·mL^{-1} solution of ^{LLL}PFF-OCH$_3$ at pH 6 with that recorded inside the droplets, upon coacervation of the same solution at pH 8.5 (Figure S4). The Raman mapping of a ^{LLL}PFF-OCH$_3$ droplet at pH 8.5 is reported in Figure 2a. The most prominent Raman feature was the sharp peak at 1003 cm^{-1}, corresponding to the phenyl ring "breathing" mode. This signal is prominent even in diluted aqueous solutions and is commonly used to normalize Raman spectra of peptides and proteins due to its relative insensitivity to the chemical environment. We used the intensity ratio between this peak and the O—H stretching band of water at ~ 3200 cm^{-1} to estimate the peptide concentration inside several droplets, which was 350 ± 30 mg·mL^{-1} (758 mM) (see Supporting Information). This corresponds to a local concentration about 38 times higher than that of the initial solution at pH 6 (10 mg·mL^{-1}, 22 mM), from which the droplets formed by increasing the pH to 8.5. This level of enrichment is consistent with the ~ 75% water content reported for similar peptide-based coacervates [10].

We then compared the six most intense Raman bands of the phenyl rings across the three aforementioned conditions. These signals, centered at 1606, 1586, 1207, 1031, 1003, and 622 cm^{-1}, referred to as F1 to F6, are typically weakly sensitive to the molecular environment [21]. As expected, their positions and intensities varied only slightly between the dilute pH 6 solution, the dense LLPS phase at pH 8.5, and the solid racemate. An exception was the 1207 cm^{-1} band (Figure 2b), whose vibrational mode involves the β-carbon of the phenylalanine side chain and is therefore more affected by the chemical environment. A progressive red shift across the three states suggests increased local packing and enhanced π–π interactions (Figure 2c; Table S1) [21].

Next, we compared the peptide backbone conformation by analyzing the amide I region in both Raman and IR spectra (Figure 2d). To avoid overlap with the H_2O bending band at 1640 cm^{-1}, we used D_2O-based solutions. Despite this, in the dilute pH 6 solution the amide I signal was indistinguishable from the noise. We therefore focused our comparison on the amide I region of the liquid droplets and the solid racemate. The IR spectrum of the enantiopure droplets displays a broad amide I band centered at 1645 cm^{-1} (FWHM ~ 53 cm^{-1}). Second-derivative analysis revealed three overlapping components centered at 1680, 1665, and 1641 cm^{-1}, consistent with disordered structures, polyproline II (pPII)-like and β-strand/turn-like conformations (Table S2) [22–24]. The corresponding Raman band displays a very broad amide I' band centered at 1660 cm^{-1} (FWHM ~ 51 cm^{-1}) featuring at least three underlying components with maxima at 1686, 1667, 1651 cm^{-1}, assigned to the same secondary structure elements [24–26]. These features suggest that the peptide adopts a highly dynamic and disordered conformational ensemble within the droplets, consistent with their liquid nature and the transient character of interpeptide interactions.

In contrast, the amide I band of the solid racemate is narrower (FWHM IR ~ 37 cm^{-1}, Raman ~ 20 cm^{-1}), with reduced contribution from disordered structures, in favor of β-strand signature. This shift reflects increased conformational order and rigidity in the solid racemate. The second peak present in the Raman (1738 cm^{-1}) and IR (1742 cm^{-1}) spectra is associated with the C=O stretching mode of the methyl ester. Also, in this case a narrowing of the FWHM is observed when moving from LLPS to the solid racemate.

Collectively, the spectroscopic data show that LLPS promotes a dynamic conformational ensemble enriched in disordered, pPII- and β-like structures, while the solid racemate adopts a more rigid and elongated conformations. This highlights how pH and enantiopurity modulate both phase behavior and peptide secondary structure.

16136829, 0, Downloaded from https://onlinelibrary.wiley.com/doi/10.1002/smll.202514872 by Giuseppe Grasso - Universita Di Catania , Wiley Online Library on [16/02/2026]. See the Terms and Conditions (https://onlinelibrary.wiley.com/terms-and-conditions) on Wiley Online Library for rules of use; OA articles are governed by the applicable Creative Commons License

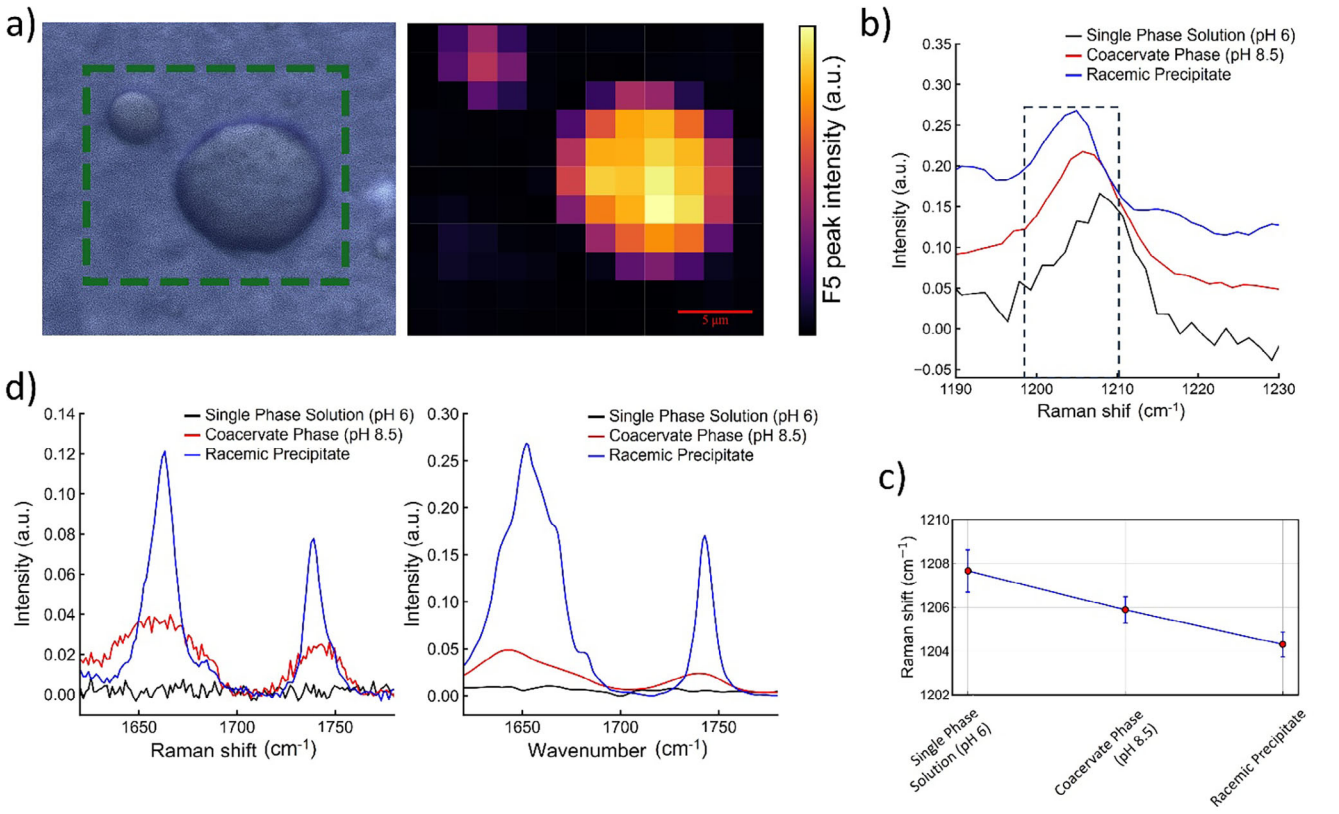

FIGURE 2 | Spectroscopic characterization of ^{LLL}PFF-OCH$_3$ under different pH conditions. a) Optical micrograph (left) of an aqueous solution at pH 8.5, showing a representative coacervate droplet (green dashed box), and the corresponding Raman intensity map (right) of the boxed region for the F5 band (1003 cm^{-1}) [21]. b) Raman spectra in H_2O highlighting the F3 band for three sample states: single phase solution (pH 6, black), coacervate phase (pH 8.5, blue), and racemic precipitate (red). c) F3 peak positions (1207 cm^{-1}) obtained by Gaussian fitting of the spectra in panel b); error bars indicate the 95% confidence interval of the fit. d) Comparison of Raman (left) and ATR-FTIR (right) spectra in D_2O for the same three sample states, focusing on the C═O stretching vibrations of the amide I band and the methyl ester group (Raman: 1738 cm^{-1}; IR: 1742 cm^{-1}).

To gain further molecular level understanding of the conformational ensemble and supramolecular organization of ^{LLL}PFF-OCH$_3$ coacervates we performed all-atom molecular dynamics (MD) simulations on the microsecond timescale (see the Supporting Information) mimicking the concentration (758 mM) inside the droplets experimentally estimated from micro-Raman data. This corresponds to a water-to-peptide ratio of approximately 75, specifically 538 peptide molecules and 39 000 water molecules were used in the simulation box. To mimic the coacervate phase, the peptides were modelled as 93% cationic and 7% neutral, reflecting an estimated pH of ~ 9.5, based on an assumed peptide pK_a of 10.6 typical of secondary amines. This mildly alkaline pH lies just above the experimentally tested range, ensuring a statistically relevant fraction of deprotonated peptides while remaining compatible with the LLPS phase diagram (Figure 1b). To maintain charge neutrality, an appropriate number of Cl^- counterions was added. To dissect the role of charge in supramolecular organization, two additional simulations were performed to represent the limiting cases of peptide protonation: one with fully protonated peptides, mimicking conditions well below the LLPS onset (Figure 1b), and another with fully deprotonated peptides, representing conditions beyond the LLPS stability range (Figure 1b,e). The fully protonated system reflects the behaviour of acidic, transparent peptide solutions, albeit at a higher concentration than in the corresponding experiment (10 mg·mL^{-1}, 22 mM), while the fully deprotonated system captures the tendency of peptides to aggregate into insoluble, solid-like particles under strongly basic conditions. In all systems, the peptides were initially randomly placed in the simulation box, ensuring full hydration of the peptides.

Visual inspection of the MD trajectories reveals increased peptide aggregation with decreasing peptide charge, indicating that reduced electrostatic repulsion allows peptides to approach more closely and interact more extensively (Figure 3a–c). Cluster analysis performed using DBSCAN [27–29] (Table S3) quantitatively shows that as the fraction of neutral peptides increases, the system transitions from many small, dispersed clusters to fewer, larger aggregates, ranging from 41 clusters on average with a mean size of 11 peptides in the fully cationic system to 13 clusters on average with a mean size of 47 peptides in the neutral system (Figure 3d–f; Figures S5–S7).

Analysis of distances between phenylalanine side chains (Figure 3g) reveals a clear increase in π–π stacking interactions between peptides as the concentration of neutral peptides rises. Quantitative assessment shows significantly more aromatic contacts within a 5.7 Å cutoff in systems containing neutral peptides, underscoring the critical role of aromatic interactions as the dominant driving force behind LLPS and aggregation of ^{LLL}PFF-OCH$_3$. Concurrently, intramolecular π–π stacking decreases. Interestingly, although the degree of aggregation

16136829, 0, Downloaded from https://onlinelibrary.wiley.com/doi/10.1002/smll.202514872 by Giuseppe Grasso - Universita Di Catania , Wiley Online Library on [16/02/2026]. See the Terms and Conditions (https://onlinelibrary.wiley.com/terms-and-conditions) on Wiley Online Library for rules of use; OA articles are governed by the applicable Creative Commons License

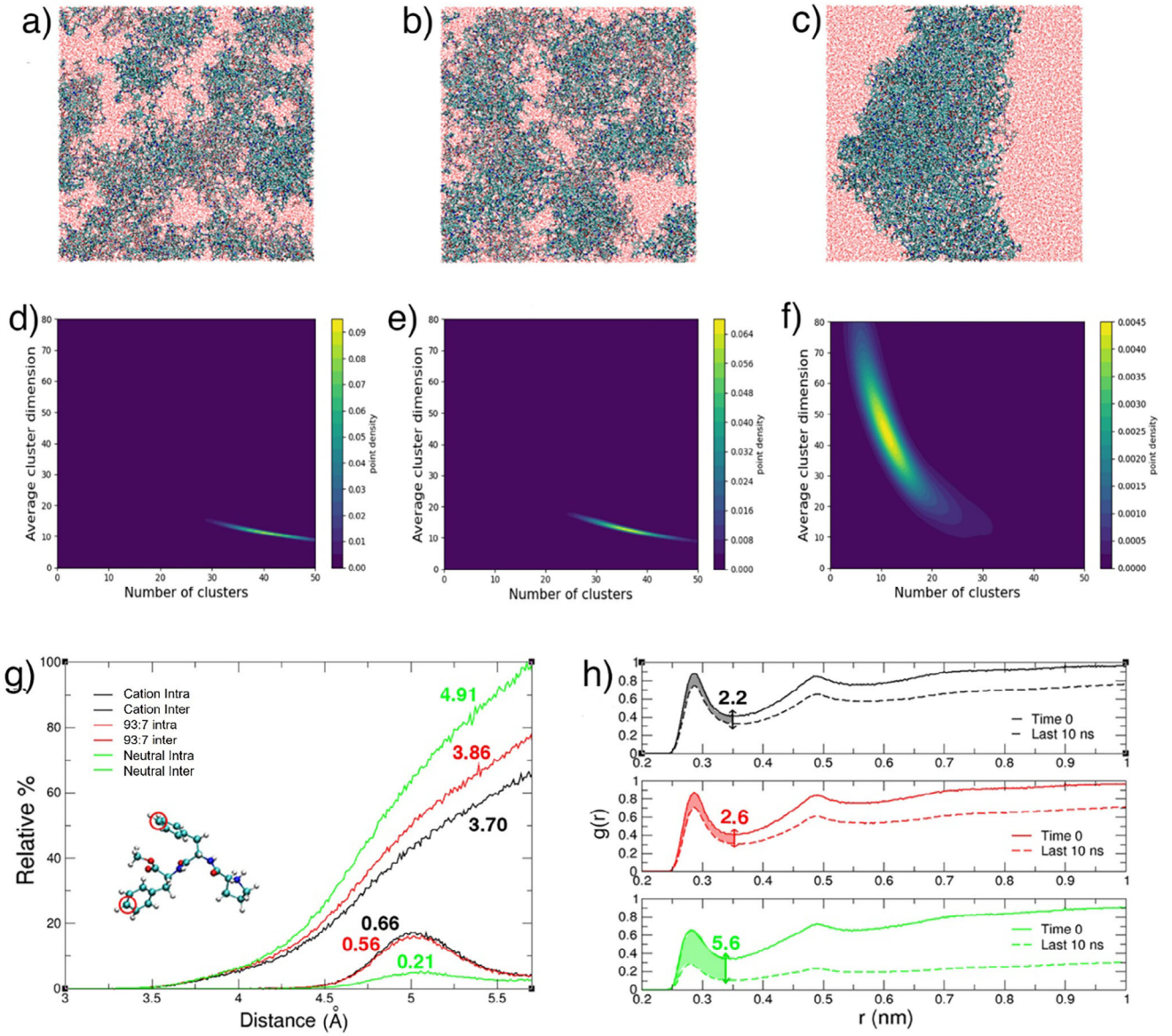

FIGURE 3 | MD simulation results. Panels a–c: Representative snapshots from MD simulations illustrating peptide aggregation in the protonated, 93:7, and deprotonated systems, respectively. Panel d-f: Contour plots showing the correlation between the number of clusters and the average cluster size in the cationic, 93:7, and neutral systems, respectively. Panel g: Distribution of intra- and inter-molecular distances between the para carbon atoms (Cε) of phenylalanine side-chain phenyl rings, truncated at the first minimum of RDF, highlighting aromatic stacking interactions in the cationic (black), 93:7 (red) and neutral (green) systems. The values highlighted in the figure represent the average number of intramolecular and intermolecular interactions per molecule within MD simulation results. Radial distribution functions (RDFs) between peptide heteroatoms and water oxygen atoms are shown for the first nanosecond and the last ten nanoseconds of the simulation for each system (black lines represent the cationic system, red lines represent the 93:7 system, and green lines represent the neutral system). These RDFs are used to compare the decrease in hydration in the three systems. The difference in the coordination number of water molecules, integrated up to the first minimum, is indicated above the double arrow.

is relatively high in all systems, the number of inter-peptide hydrogen bonds remains consistently low, amounting to 0.13, 0.15, and 0.47 per peptide in the fully cationic, 93:7 cationic:neutral, and fully neutral systems, respectively, (Figure S8) suggesting that aggregation is not primarily driven by hydrogen bonding.

Analysis of the φ/ψ dihedral angles (Figure S9) reveals that the backbone conformations cluster into three main basins: a broad basin centered at around −67°/140°, characteristic of polyproline II (pPII) conformations; a second basin centered at around −139°/150°, indicative of β-sheet–like conformations; and a third basin centered at around −66°/−43°, corresponding to turn-like conformations. Within the coacervate phase, the most populated basin is the pPII one, followed by the turn-like basin, with a minor contribution from the β-sheet–like basin. In the fully neutral system, the population of the β-sheet-like basin increases at the expense of the pPII and turn-like basins. These results indicate that the conformational repertoire within the coacervate phase is heterogeneous and largely disordered, lacking well-defined secondary structural elements, consistent with the observations from IR and Raman spectroscopy, and in line with previous work on similar systems [6, 7].

16136829, 0, Downloaded from https://onlinelibrary.wiley.com/doi/10.1002/smll.202514872 by Giuseppe Grasso - Universita Di Catania , Wiley Online Library on [16/02/2026]. See the Terms and Conditions (https://onlinelibrary.wiley.com/terms-and-conditions) on Wiley Online Library for rules of use; OA articles are governed by the applicable Creative Commons License

We finally examine the degree of peptide hydration in the coacervates and compare it to the fully cationic and fully neutral systems. Analysis of the radial distribution functions (RDFs) between peptide heteroatoms and water oxygens (Figure 3h) shows that hydration levels in the coacervates remain high, as evidenced by the pronounced first peak in the RDF, which is similar to that observed in the fully cationic system (Figure S10). The coordination number within the first hydration shell (up to the first minimum) is in fact 9.6 and 10.2 for the coacervate and fully cationic system, respectively. In contrast, comparison with the fully neutral system reveals a significant expulsion of water molecules from the peptide environment as neutrality increases, reflected by the overall decrease in the RDF intensity across the entire distance range. Specifically, the decrease in water coordination number from the fully dispersed state (i.e., at the start of the MD trajectories) to the equilibrated phase of the simulation becomes more pronounced when moving from the fully cationic system (in which the decrease is 2.2) to the fully neutral one (in which the decrease is 5.6).

These findings collectively support a model in which the reduced electrostatic repulsion resulting from an increased fraction of neutral peptides relative to cationic ones facilitates aromatic-driven aggregation, leading to fewer but larger peptide clusters. Altogether, these results highlight the critical interplay between peptide charge state, conformation, and supramolecular interactions that underpins the formation and stability of peptide-based coacervates.

To directly assess how enantiopurity affects the aggregation, we also performed long-timescale MD simulations of the racemic system. We repeated the simulation of the enantiopure ^{LLL}PFF-OCH$_3$ coacervates (93% cationic and 7% neutral peptides) but with half of the peptides replaced by the D-enantiomer ^{DDD}PFF-OCH$_3$. All other parameters were identical. At the level of global observables, the racemic and enantiopure systems exhibited comparable average structural properties within statistical uncertainty, including Ramachandran φ/ψ distributions, Phe–Phe side-chain contact probabilities, overall hydrogen-bond populations, and number of water molecules hydrating the peptides. However, when focusing on the subset of peptide pairs connected by intermolecular backbone hydrogen bonds, clear microscopic differences emerged. In the enantiopure L system, hydrogen-bonded dimers preferentially adopted incipient antiparallel pleated β-sheet arrangements, whereas in the racemic system they reorganized into a distinct motif consistent with the "rippled" β-sheet architecture (Figure S12) described in the literature [30]. This difference is quantitatively captured by the distribution of the angle between the Cα–Cβ vectors of the central phenylalanine in hydrogen-bonded peptide dimers, which peaks at $\sim 42°$ in the enantiopure system, in line with antiparallel pleated β-sheets, and is shifted to $\sim 154°$ in the racemic system, matching the geometry expected for rippled sheets (Figure S12). These simulations therefore support a scenario in which the alternation of L and D peptide enantiomers disrupts the regular side-chain alternation characteristic of pleated β-sheets and instead promotes more irregular, asymmetric side-chain packing, in agreement with recent reports showing that racemic peptides of diverse length and composition tend to precipitate into rippled β-sheets rather than classical pleated β-structures [31, 32].

Encouraged by the robust LLPS behavior of ^{LLL}PFF-OCH$_3$ and the ability of their droplets to solubilize organic molecules, such as rhodamine B during our FRAP experiments, we investigated whether these peptide droplets could function as confined chiral microreactors for enantioselective organocatalysis. In fact, rhodamine B exhibited a partition coefficient of 144:1 between ^{LLL}PFF-OCH$_3$ coacervate and the dilute phases (Figure S10), consistent with previous reports for ^{LL}FF-OCH$_3$ droplets [10]. The prominent role that peptides have in asymmetric catalysis is majorly due to their unique combination of modularity and tunability. Synthetic peptides, particularly those of low molecular weight, can be easily prepared and customized by altering amino acid sequences, enabling fine-tuning of their structural and catalytic features [33]. Their ability to adopt well-defined secondary structures allows for the precise spatial arrangement of functional groups, thereby promoting highly selective substrate activation [34] and control over point, axial, and conformational chirality [35]. Creating a chiral lipophilic microenvironment is indeed recognized as a good strategy to achieve (enantio)selective transformations [13]. As a proof of concept, we tested the aldol reaction between cyclohexanone and benzaldehyde (Figure 4), a transformation known to be enantioselectively catalyzed by proline [36–38], and proline-containing peptides, with catalytic efficiency often depending on their supramolecular organization [13, 39]. These two otherwise water-insoluble aldol substrates are solubilized within the ^{LLL}PFF-OCH$_3$ coacervate droplets, as confirmed by Micro-Raman spectroscopy (Figure S13).

We compared the catalytic properties of enantiopure ^{LLL}PFF-OCH$_3$ droplets to the droplets formed from the ^{LL}FF-OCH$_3$ dipeptide. Reactions were conducted using 20 mol% of catalyst at pH 8.5 and 4°C for 20 h to ensure droplet density and stability. The catalytic experiments are conducted under conditions where the coacervate droplets are persistent over the full reaction time (Figure 1j). The ^{LL}FF-OCH$_3$ droplets proved competent for catalyzing the aldol reaction, in agreement with previous reports on similar ^{LL}FF-OCH$_3$-based coacervates [10]. Interestingly, HPLC analysis of the β-hydroxy ketone product revealed that ^{LL}FF-OCH$_3$ droplets, despite lacking proline functionality, but thanks to a free amino group, can function as chiral microreactors, albeit with moderate enantioselectivity (ee = 38%). Notably, the ^{LLL}PFF-OCH$_3$ droplets outperformed the ^{LL}FF-OCH$_3$ ones in both diastereo- and enantioselectivity (Figure 4). We attribute this enhancement to the presence of the N-terminal proline, which promotes the formation of more sterically hindered enamine intermediates, offering improved stereochemical control [40]

In short, these results highlight that ^{LLL}PFF-OCH$_3$ coacervates encapsulate organic molecules enabling asymmetric organocatalysis where N-terminal proline enhance the stereochemical control.

3 | Conclusion

Our study demonstrates that the tripeptide ^{LLL}PFF-OCH$_3$ forms liquid droplets through enantiopurity-dependent LLPS, revealing spontaneous stereochemical self-disproportionation. The racemic mixtures preferentially sample local arrangements compatible with rippled β-sheets, highlighting a chiral-sensitive

16136829, 0, Downloaded from https://onlinelibrary.wiley.com/doi/10.1002/smll.202514872 by Giuseppe Grasso - Universita Di Catania , Wiley Online Library on [16/02/2026]. See the Terms and Conditions (https://onlinelibrary.wiley.com/terms-and-conditions) on Wiley Online Library for rules of use; OA articles are governed by the applicable Creative Commons License

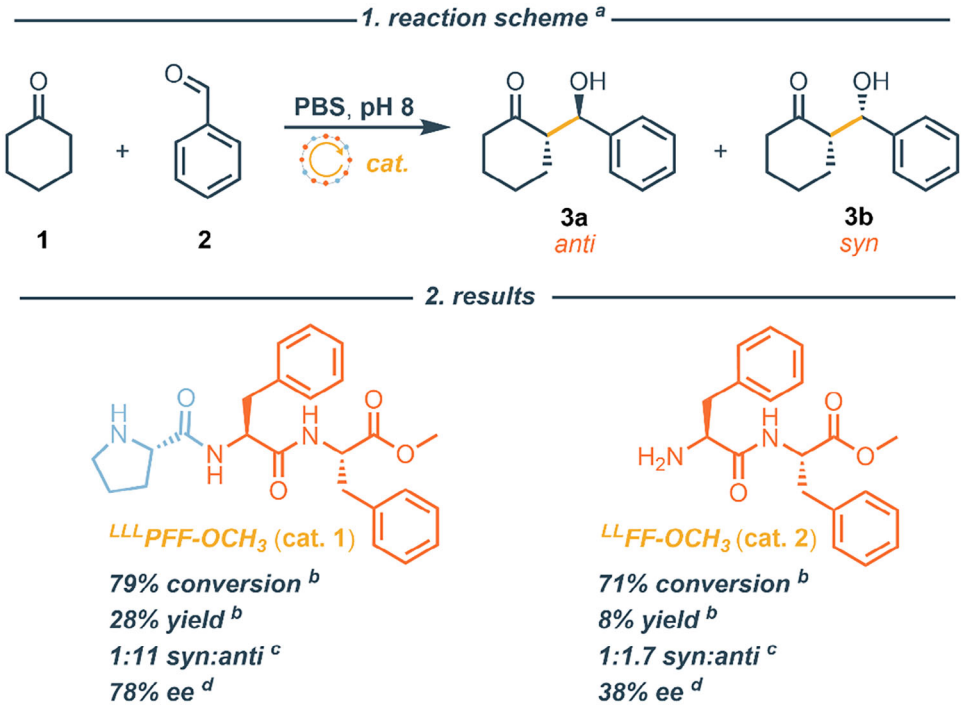

FIGURE 4 | Peptide catalysed aldol reaction. 1. reaction scheme; 2. results of the catalysed reaction. [a] All reactions were performed with **2** (11.6 mg, 0.1 mmol, 1 equiv), **1** (21.4 mg, 0.2 mmol, 2 equiv), and **cat**. (0.02 mmol, 0.2 equiv) into a PBS aqueous solution (1 mL, 0.1 M) at pH 8.5, for 20 h at 4°C. [b] Determined by ^{1}H NMR using triphenylmethane as internal standard. [c] Diasteromeric ratio of the syn:anti β-hydroxy ketone **3a** and **3b** product determined by ^{1}H NMR analysis of the crude mixture. [d] Enantiomeric excess of the major anti diasteroisomer **3a** determined by chiral HPLC analysis.

aggregation landscape. Spectroscopic analyses and molecular simulations unveiled that droplet formation relates to a dynamic and heterogeneous conformational ensemble and to hydrophobic-driven interactions, modulated by the pH. Remarkably, these peptide droplets function as chiral microreactors, for enantioselective aldol reaction. In this work, the asymmetric aldol reaction is employed as a proof of concept to demonstrate that enantiopure peptide coacervates are competent chiral organocatalytic compartments. Our findings highlight a fundamental link between molecular chirality and the spontaneous occurrence of LLPS of peptides in aqueous environments. The enantiopurity dependence observed for ^{LLL}PFF-OCH$_3$ and ^{LL}FF-OCH$_3$ LLPS suggests that it may be an essential prerequisite for the formation of stable biomolecular coacervates. This, together with the enantioselective catalytic capabilities of these liquid coacervates, is particularly intriguing from a prebiotic chemistry perspective, as early compartmentalization and selective molecular enrichment, driven by chirality-dependent LLPS, could have played a role in the emergence of homochirality [3, 41]. Furthermore, the chirality-sensitive LLPS we describe may offer significant implications for understanding pathological processes in neurodegenerative diseases. Dysregulated LLPS and protein aggregation contribute to the pathology of disorders such as Alzheimer's and Parkinson's diseases [42, 43]. While speculative, this chirality-sensitive LLPS may also be relevant in biological contexts where the dysregulations of LLPS and aggregation of proteins are implicated in diseases [44, 45]. Our results, showing that enantiopurity affects peptide LLPS behavior, suggest that similar chirality-dependent mechanisms might underline protein misfolding and aggregation in neurodegenerative pathologies.

Acknowledgements

Armando Carlone and Claudio Iacobucci acknowledge funding by the European Union—NextGenerationEU under the Italian Ministry of University and Research (MUR) National Innovation Ecosystem grant ECS00000041 – VITALITY—CUP E13C22001060006. Alessio Carioscia acknowledges Dipharma Francis for supporting his PhD fellowship. Martina Porco acknowledges Fresenius Kabi iPSUM for supporting her PhD fellowship. Claudio Iacobucci acknowledges financial support by the Italian Ministry of University and Research (MUR) (PRIN 2022 – Project 20225HNCZK) and the European Union Next Generation EU (PRIN 2022 PNRR—Project P20224WAME). Armando Carlone acknowledges financial support by the European Union Next Generation EU (PRIN 2022 PNRR—Project P2022YM7F2).

Open access publishing facilitated by Universita degli Studi dell'Aquila, as part of the Wiley - CRUI-CARE agreement.

Conflicts of Interest

The authors declare no conflicts of interest.

Data Availability Statement

The data that support the findings of this study are available in the supplementary material of this article.

References

1. S. Alberti, A. Gladfelter, and T. Mittag, "Considerations and Challenges in Studying Liquid-Liquid Phase Separation and Biomolecular Condensates," *Cell* 176 (2019): 419–434, https://doi.org/10.1016/j.cell.2018.12.035.

16136829, 0, Downloaded from https://onlinelibrary.wiley.com/doi/10.1002/smll.202514872 by Giuseppe Grasso - Universita Di Catania , Wiley Online Library on [16/02/2026]. See the Terms and Conditions (https://onlinelibrary.wiley.com/terms-and-conditions) on Wiley Online Library for rules of use; OA articles are governed by the applicable Creative Commons License

2. S. Lim and D. S. Clark, "Phase-Separated Biomolecular Condensates for Biocatalysis," *Trends in Biotechnology* 42 (2024): 496–509, https://doi.org/10.1016/j.tibtech.2023.10.003.

3. M. Abbas, W. P. Lipiński, J. Wang, and E. Spruijt, "Peptide-Based Coacervates as Biomimetic Protocells," *Chemical Society Reviews* 50 (2021): 3690–3705, https://doi.org/10.1039/D0CS00307G.

4. Y. Sun, X. Wu, J. Li, C. S. Verma, J. Yu, and A. Miserez, "Peptide-Based Complex Coacervates Stabilized by Cation–π Interactions for Cell Engineering," *Journal of the American Chemical Society* 147 (2025): 4284–4295, https://doi.org/10.1021/jacs.4c14469.

5. J. Lim, S. Gudlur, C. Buchanan, et al., "Hierarchical Structural Organization in Bioinspired Peptide Coacervate Microdroplets," *ACS Nano* 19 (2025): 35724–35739, https://doi.org/10.1021/acsnano.5c12015.

6. S. Cao, G. Li, P. Zhou, E. Gazit, X. Yan, and C. Yuan, "Entropy-Driven Amino Acid-Based Coacervates with Enzyme-Free Metabolism and Prebiotic Robustness," *Journal of the American Chemical Society* 147 (2025): 45324–45336, https://doi.org/10.1021/jacs.5c15328.

7. C. Yuan, A. Levin, W. Chen, et al., "Nucleation and Growth of Amino Acid and Peptide Supramolecular Polymers Through Liquid–Liquid Phase Separation," *Angewandte Chemie International Edition* 58 (2019): 18116–18123, https://doi.org/10.1002/anie.201911782.

8. S. Cao, T. Ivanov, J. Heuer, C. T. J. Ferguson, K. Landfester, and L. da Silva, "Dipeptide Coacervates as Artificial Membraneless Organelles for Bioorthogonal Catalysis," *Nature Communications* 15 (2024): 39, https://doi.org/10.1038/s41467-023-44278-9.

9. S. Cao, P. Zhou, G. Shen, et al., "Binary Peptide Coacervates as an Active Model for Biomolecular Condensates," *Nature Communications* 16 (2025): 2407, https://doi.org/10.1038/s41467-025-57772-z.

10. M. Abbas, W. P. Lipiński, K. K. Nakashima, W. T. S. Huck, and E. Spruijt, "A Short Peptide Synthon for Liquid–Liquid Phase Separation," *Nature Chemistry* 13 (2021): 1046–1054.

11. B. Lewandowski and H. Wennemers, "Asymmetric Catalysis With Short-chain Peptides," *Current Opinion in Chemical Biology* 22 (2014): 40–46, https://doi.org/10.1016/j.cbpa.2014.09.011.

12. O. Zozulia, M. A. Dolan, and I. V. Korendovych, "Catalytic Peptide Assemblies," *Chemical Society Reviews* 47 (2018): 3621–3639, https://doi.org/10.1039/C8CS00080H.

13. A. Sinibaldi, F. Della Penna, M. Ponzetti, et al., "Asymmetric Organocatalysis Accelerated via Self-Assembled Minimal Structures," *European Journal of Organic Chemistry* 2021 (2021): 5403–5406, https://doi.org/10.1002/ejoc.202101042.

14. S. L. Perry, L. Leon, K. Q. Hoffmann, et al., "Chirality-selected Phase Behaviour in Ionic Polypeptide Complexes," *Nature Communications* 6 (2015): 6052, https://doi.org/10.1038/ncomms7052.

15. G. A. Zingale, I. Pandino, D. Calcagno, M. L. Perina, N. Tuccitto, and G. Grasso, "Label-Free Determination of Diffusion Coefficients at the Nanoscale Through Modelling of the Surface Plasmon Resonance Signal," *PLoS ONE* 20 (2025): 0312594, https://doi.org/10.1371/journal.pone.0312594.

16. G. S. Basile, D. Calcagno, N. Tuccitto, D. Sbardella, and G. Grasso, "Broad-Spectrum Diffusion Coefficient Measurements via Surface Plasmon Resonance: From Thermodynamics to Protein Conformational Disorders," *ChemPhysChem* 26 (2025): 2500138.

17. D. Calcagno, M. L. Perina, A. Distefano, et al., "Albumin Folding Changes Affect the Microfluidic Interfacial Broadening Revealed by Surface Plasmon Resonance," *Chemistry–Methods* 5 (2025): 202400034, https://doi.org/10.1002/cmtd.202400034.

18. T. Mittag and R. Parker, "Multiple Modes of Protein–protein Interactions Promote RNP Granule Assembly," *Journal of Molecular Biology* 430 (2018): 4636–4649.

19. J. Han, O. Kitagawa, A. Wzorek, K. D. Klika, and V. A. Soloshonok, "The Self-Disproportionation of Enantiomers (SDE): A Menace or an Opportunity?," *Chemical Science* 9 (2018): 1718–1739, https://doi.org/10.1039/C7SC05138G.

20. M. Klussmann, H. Iwamura, S. P. Mathew, et al., "Thermodynamic Control of Asymmetric Amplification in Amino Acid Catalysis," *Nature* 441 (2006): 621–623, https://doi.org/10.1038/nature04780.

21. B. Hernández, F. Pflüger, S. G. Kruglik, and M. Ghomi, "Characteristic Raman Lines of Phenylalanine Analyzed by a Multiconformational Approach," *Journal of Raman Spectroscopy* 44 (2013): 827–833, https://doi.org/10.1002/jrs.4290.

22. M. Martino, A. Bavoso, V. Guantieri, A. Coviello, and A. M. Tamburro, "On the Occurrence of Polyproline II Structure in Elastin," *Journal of Molecular Structure* 519 (2000): 173–189, https://doi.org/10.1016/S0022-2860(99)00299-9.

23. J. Kong and S. Yu, "Fourier Transform Infrared Spectroscopic Analysis of Protein Secondary Structures," *Acta Biochimica et Biophysica Sinica* 39 (2007): 549–559, https://doi.org/10.1111/j.1745-7270.2007.00320.x.

24. C. R. Jacob, S. Luber, and M. Reiher, "Analysis of Secondary Structure Effects on the IR and Raman Spectra of Polypeptides in Terms of Localized Vibrations," *The Journal of Physical Chemistry B* 113 (2009): 6558–6573, https://doi.org/10.1021/jp900354g.

25. J. L. Lippert, D. Tyminski, and P. J. Desmeules, "Determination of the Secondary Structure of Proteins by Laser Raman Spectroscopy," *Journal of the American Chemical Society* 98 (1976): 7075–7080, https://doi.org/10.1021/ja00438a057.

26. N. C. Maiti, M. M. Apetri, M. G. Zagorski, P. R. Carey, and V. E. Anderson, "Raman Spectroscopic Characterization of Secondary Structure in Natively Unfolded Proteins: α-Synuclein," *Journal of the American Chemical Society* 126 (2004): 2399–2408, https://doi.org/10.1021/ja0356176.

27. A. Semmeq, S. Del Galdo, M. Chiarini, I. Daidone, and C. Casieri, "Structural and Dynamic Behaviour of Concentrated Aqueous Solutions of (poly) Ethylene Glycols: Insight into the Impact of Hydrophobicity, Hydrogen Bonding and Chain Length," *Journal of Molecular Liquids* 411 (2024): 125654, https://doi.org/10.1016/j.molliq.2024.125654.

28. J. Bachler, I. Daidone, L. Zanetti-Polzi, and T. Loerting, "Tuning the Low-Temperature Phase Behavior of Aqueous Ionic Liquids," *Physical Chemistry Chemical Physics* 26 (2024): 9741–9753, https://doi.org/10.1039/D3CP06101A.

29. A. Semmeq, S. Del Galdo, M. Chiarini, I. Daidone, and C. Casieri, "Macromolecular vs Molecular Crowding in Aqueous Solutions: A Comparative Study of PEG400 and Ethylene Glycol," *Journal of Molecular Liquids* 394 (2024): 123713, https://doi.org/10.1016/j.molliq.2023.123713.

30. A. Hazari, M. R. Sawaya, H. Lee, et al., "Formation of Rippled β-Sheets from Mixed Chirality Linear and Cyclic Peptides—New Structural Motifs Based on the Pauling-Corey Rippled β-Sheet," *Chemical Science* 16 (2025): 5907–5917.

31. A. Hazari, M. R. Sawaya, M. Sajimon, et al., "Racemic Peptides From Amyloid β and Amylin Form Rippled β-sheets Rather Than Pleated β-sheets," *Journal of the American Chemical Society* 145 (2023): 25917–25926, https://doi.org/10.1021/jacs.3c11712.

32. A. J. Kuhn, B. Ehlke, T. C. Johnstone, S. R. J. Oliver, and J. A. Raskatov, "A Crystal-structural Study of Pauling–Corey Rippled Sheets," *Chemical Science* 13 (2022): 671–680.

33. J. Nowag, M. Brauser, L. Steuernagel, R. C. Wende, P. R. Schreiner, and C. M. Thiele, "Quantifying Intermolecular Interactions in Asymmetric Peptide Organocatalysis as a Key Toward Understanding Selectivity," *Journal of the American Chemical Society* 146 (2023): 170–180, https://doi.org/10.1021/jacs.3c06378.

34. K. Kudo, "Asymmetric Peptide Catalysis," in *Catalytic Asymmetric Synthesis*. (Eds: T. Akiyama, I. Ojima), (Wiley, 2022): pp. 157–198, https://doi.org/10.1002/9781119736424.ch5.

16136829, 0, Downloaded from https://onlinelibrary.wiley.com/doi/10.1002/smll.202514872 by Giuseppe Grasso - Universita Di Catania , Wiley Online Library on [16/02/2026]. See the Terms and Conditions (https://onlinelibrary.wiley.com/terms-and-conditions) on Wiley Online Library for rules of use; OA articles are governed by the applicable Creative Commons License

35. A. J. Metrano, A. J. Chinn, C. R. Shugrue, E. A. Stone, B. Kim, and S. J. Miller, "Asymmetric Catalysis Mediated by Synthetic Peptides, Version 2.0: Expansion of Scope and Mechanisms," *Chemical Reviews* 120 (2020): 11479–11615, https://doi.org/10.1021/acs.chemrev.0c00523.

36. B. List, R. A. Lerner, and C. F. Barbas, "Proline-catalyzed Direct Asymmetric Aldol Reactions," *Journal of the American Chemical Society* 122 (2000): 2395–2396, https://doi.org/10.1021/ja994280y.

37. G. Di Carmine, F. Pesciaioli, S. Wang, et al., "Insights into Substituent Effects of Benzaldehyde Derivatives in a Heterogeneous Organocatalyzed Aldol Reaction," *Chemcatchem* 14 (2022): 202200405, https://doi.org/10.1002/cctc.202200405.

38. G. Di Carmine, L. Forster, S. Wang, C. Parlett, A. Carlone, and C. D'agostino, "NMR Relaxation Time Measurements of Solvent Effects in an Organocatalysed Asymmetric Aldol Reaction Over Silica SBA-15 Supported Proline," *Reaction Chemistry & Engineering* 7 (2022): 269–274, https://doi.org/10.1039/D1RE00471A.

39. H. Wennemers, "Asymmetric Catalysis with Peptides," *Chemical Communications* 47 (2011): 12036, https://doi.org/10.1039/c1cc15237h.

40. S. Bahmanyar, K. N. Houk, H. J. Martin, and B. List, "Quantum Mechanical Predictions of the Stereoselectivities of Proline-Catalyzed Asymmetric Intermolecular Aldol Reactions," *Journal of the American Chemical Society* 125 (2003): 2475–2479, https://doi.org/10.1021/ja028812d.

41. A. Sathyavageeswaran, J. Bonesso Sabadini, and S. L. Perry, "Self-Assembling Polypeptides in Complex Coacervation," *Accounts of Chemical Research* 57 (2024): 386–398, https://doi.org/10.1021/acs.accounts.3c00689.

42. S. Mukherjee, M. Poudyal, K. Dave, P. Kadu, and S. K. Maji, "Protein Misfolding and Amyloid Nucleation Through Liquid–Liquid Phase Separation," *Chemical Society Reviews* 53 (2024): 4976–5013.

43. A. Zbinden, M. Pérez-Berlanga, P. De Rossi, and M. Polymenidou, "Phase Separation and Neurodegenerative Diseases: A Disturbance in the Force," *Developmental Cell* 55 (2020): 45–68, https://doi.org/10.1016/j.devcel.2020.09.014.

44. Y. Zheng, K. Mao, S. Chen, and H. Zhu, "Chirality Effects in Peptide Assembly Structures," *Frontiers in Bioengineering and Biotechnology* 9 (2021): 703004, https://doi.org/10.3389/fbioe.2021.703004.

45. S. H. More, T. Dorosh, J.-Y. Runser, et al., "Influence of Peptide Chirality on Their Protein-Triggered Supramolecular Hydrogelation," *Faraday Discussions* 260 (2025): 310–327, https://doi.org/10.1039/D5FD00007F.

Supporting Information

Additional supporting information can be found online in the Supporting Information section.

Supporting File: smll72760-sup-0001-SuppMat.pdf.

16136829, 0, Downloaded from https://onlinelibrary.wiley.com/doi/10.1002/smll.202514872 by Giuseppe Grasso - Universita Di Catania , Wiley Online Library on [16/02/2026]. See the Terms and Conditions (https://onlinelibrary.wiley.com/terms-and-conditions) on Wiley Online Library for rules of use; OA articles are governed by the applicable Creative Commons License